Microscopic approach of fission dynamics applied to fragment kinetic energy and mass distributions in ^{238}U

H. Goutte,* J. F. Berger, P. Casoli, and D. Gogny†
CEA/DAM Ile de France DPTA/Service de Physique Nucléaire, BP 12, F-91680 Bruyères-le-Châtel, France
(Received 22 July 2004; published 28 February 2005)

The collective dynamics of low-energy fission in ^{238}U is described within a time-dependent formalism based on the Gaussian overlap approximation of the time-dependent generator coordinate method. The intrinsic deformed configurations of the nucleus are determined from the self-consistent Hartree-Fock-Bogoliubov procedure employing the effective force D1S with constraints on the quadrupole and octupole moments. Fragment kinetic energy and mass distributions are calculated and compared with experimental evaluations. The effect of the collective dynamics along the fission paths and the influence of initial conditions on these distributions are analyzed and discussed.

DOI: 10.1103/PhysRevC.71.024316 PACS number(s): 21.60.Jz, 21.60.Ev, 24.75.+i, 25.85.−w

I. INTRODUCTION

Interest in fission has recently increased since it is proposed to be used in new applications such as accelerator-driven systems, new electro-nuclear cycles such as a thorium-based fuel cycle, and the next generation of exotic beam facilities. For these applications, there is an important need for fission cross sections in a large range of excitation energies and for mass-charge fission fragment distributions. For instance, precise knowledge of production rates of secondary long-lived fission residues and of neutron-rich isotopes is crucial for designing and simulating these new facilities. It is worth pointing out that relevant measurements of mass and charge distributions have been performed recently. For instance, the production of exotic nuclei has been measured from spallation reactions of 1*A* GeV ^{238}U projectiles on a hydrogen target [1] and isotopic yields have been deduced for elements between ^{58}Ni and ^{163}Eu. Furthermore, thanks to secondary beam facilities, fission properties of 70 short-lived radioactive nuclei can be found in Refs. [2,3]. Such a systematic analysis of the fission properties covers a wide region of the nuclide chart, and the transition between single- and double-humped mass distributions has been observed with a triple-humped structure for ^{227}Th. It is important to test the accuracy of a theoretical prediction using data in order to gain confidence in its predictions when applied to widely extended domains such as the fission of nuclei far from stability and fission for a large range of excitation energies.

From a theoretical point of view, the description of the fission process stands at the crossroads of many subjects in the forefront of research. Both static and dynamic properties of the fissioning system are required, namely, nuclear configurations far from equilibrium, the interplay of collective and intrinsic degrees of freedom, and the dynamics of large-amplitude collective motion. Theoretical works generally focus on the static part of fission. For instance, many studies have been devoted to multidimensional potential energy surfaces [4,5] from which fission barriers are extracted and to nuclear configurations at scission and associated fragment distributions [6,7]. On the other hand, there are very few dynamic studies of fission, although dynamic effects are expected to play an essential role in the process, particularly in the descent from saddle to scission. Fragment mass distributions have recently been obtained by solving the classical three-dimensional Langevin equations [8]. The influence of the mass asymmetry degree of freedom on the variance of the mass distribution has been highlighted. Two types of microscopic quantum dynamic calculations have also been performed in the past. First, in 1978, the time-dependent Hartree-Fock method [9] was applied to fission. Second, time-dependent calculations based on the generator coordinate method using Hartree-Fock-Bogoliubov states were performed, and the most probable fission configuration of ^{240}Pu was analyzed [10]. The present study is an extension of this pioneering work.

In the present work, we have chosen to derive the collective dynamics of fission using a time-dependent formalism based on the Gaussian overlap approximation of the time-dependent generator coordinate (GC) theory. An alternative method could have been to first determine the stationary solutions of the GC equations within the relevant domain of generator coordinates with appropriate boundary conditions. The solutions of the time-dependent GC equations would then be expressed in a straightforward manner. However, the precise form of the boundary conditions to be used is difficult to obtain when more than one generator coordinates is employed. Applying a time-dependent method allows one to avoid this problem. The only input of the calculation is the collective wave function chosen at $t = 0$. Spurious reflections of the time-dependent collective wave function at the edge of the finite domain are eliminated using a standard absorption technique as explained in Sec. III.

In this paper, we focus on low-energy fission-fragment distributions of ^{238}U and on several physical aspects that can be clearly analyzed in this even-even fissioning system. Let us recall that at low energy, elongation and asymmetry degrees of freedom are among the most relevant ones and that the

*E-mail address: heloise.goutte@cea.fr
†Present address: L-414 Lawrence Livermore National Laboratory, Livermore, California 94551.

 ©2005 The American Physical Society

adiabatic assumption is to a large extent justified [11]. As we explain later, time evolution in the fission channel is described in terms of a wave function of Hill-Wheeler type. The latter is taken as a linear combination of the Hartree-Fock-Bogoliubov (HFB) solutions characterized by the two collective degrees of freedom just mentioned. It is worth pointing out that this work relies only on the D1S effective interaction used at Bruyères-le-Châtel.

The calculation proceeds in two steps: first the potential energy surface and the collective inertia are determined from the first well to scission, and then the dynamic treatment of fission is performed using an approximate time-dependent generator coordinate method (TDGCM). Potential energy surfaces and associated collective inertia tensors are calculated using the constrained Hartree-Fock-Bogoliubov approach with the D1S finite-range effective force [12,13]. Fission wave functions at time zero are constructed from the quasistationary collective states in the first well. Their time evolution is calculated numerically by discretizing on a mesh a time-dependent Schrödinger-like equation. Mass distributions are derived from the flux of the wave function through scission at given A_H/A_L fragmentations.

The present work is organized as follows. The HFB formalism and the TDGCM method are presented in Sec. II and numerical procedures are detailed in Sec. III. Section IV is devoted to the static results, where the potential energy surface and pairing correlations are discussed. A first estimate of kinetic energy and fragment mass distributions, obtained from a "static" calculation at scission, are discussed. Mass distributions obtained from the full time-dependent calculations are presented in Sec. V, and the crucial role played by dynamic effects is analyzed.

II. FORMALISM

In low-energy fission, the adiabatic hypothesis seems to be justified [11] and, therefore, collective and intrinsic degrees of freedom can be decoupled. Furthermore, we assume that the collective motion of the system can be described in terms of a few collective variables characterizing the shape evolution of the nucleus. In a self-consistent formalism, these shapes can be generated by means of external fields represented by the operators

$$\hat{Q}_{20} = \sqrt{\frac{16\pi}{5}} \sum_{i=1}^{A} r_i^2 Y_{20} = \sum_{i=1}^{A} \left(2z_i^2 - x_i^2 - y_i^2\right), \qquad (1)$$

and

$$\hat{Q}_{30} = \sqrt{\frac{4\pi}{7}} \sum_{i=1}^{A} r_i^3 Y_{30} = \sum_{i=1}^{A} \left[z_i^3 - \frac{3}{2} z_i \left(x_i^2 + y_i^2\right)\right]. \qquad (2)$$

These moments govern mass axial deformation and left-right asymmetry of the nucleus, respectively. For well-separated fragments, we can express the mean values of these operators in terms of $\langle Q_{20}^H \rangle (\langle Q_{30}^H \rangle)$ and $\langle Q_{20}^L \rangle (\langle Q_{30}^L \rangle)$, the mean quadrupole (octupole) deformations of the heavy and light fragments, respectively; d_m the distance between their centers of mass; and μ the reduced mass, such that

$$\begin{aligned} \langle Q_{20} \rangle &= \langle Q_{20}^H \rangle + \langle Q_{20}^L \rangle + 2\mu d_m^2, \\ \langle Q_{30} \rangle &= \langle Q_{30}^H \rangle + \langle Q_{30}^L \rangle + \frac{3d_m}{A_H + A_L} \left(A_H \langle Q_{20}^L \rangle - A_L \langle Q_{20}^H \rangle\right) \\ &\quad + 2\mu d_m^3 \frac{A_H - A_L}{A_H + A_L}, \end{aligned} \qquad (3)$$

with

$$\mu = \frac{A_H A_L}{A_H + A_L}. \qquad (4)$$

Relations (3) and (4) have only been used in the present work to check the validity of the computer program for configurations close to scission.

The intrinsic axially deformed states $|\Phi(q_{20}, q_{30})\rangle$ of the fissile system are taken as the solutions of the constrained Hartree-Fock-Bogoliubov variational principle [13]

$$\begin{aligned} &\delta \langle \Phi(q_{20}, q_{30}) | \hat{H} - \lambda_N \hat{N} - \lambda_Z \hat{Z} \\ &\quad - \sum_i \lambda_i \hat{Q}_i | \Phi(q_{20}, q_{30}) \rangle = 0, \end{aligned} \qquad (5)$$

where the Lagrange parameters λ_N, λ_Z, and λ_i are deduced from

$$\begin{aligned} \langle \Phi(q_{20}, q_{30}) | \hat{N} | \Phi(q_{20}, q_{30}) \rangle &= N, \\ \langle \Phi(q_{20}, q_{30}) | \hat{Z} | \Phi(q_{20}, q_{30}) \rangle &= Z, \end{aligned} \qquad (6)$$

and

$$\langle \Phi(q_{20}, q_{30}) | \hat{Q}_i | \Phi(q_{20}, q_{30}) \rangle = q_i.$$

In Eq. (5), $\hat{Q}_i$ is the set of external field operators ($\hat{Q}_{20}$, $\hat{Q}_{30}$, $\hat{Q}_{10}$), and $\hat{H}$ is the nuclear many-body effective Hamiltonian built with the finite-range effective force D1S [13]. The additional constraint on the dipole mass operator is used to fix the position of the center of mass of the whole system. This is accomplished by setting $\langle \hat{Q}_{10} \rangle = 0$, where

$$\hat{Q}_{10} = \sqrt{\frac{4\pi}{3}} \sum_{i=1}^{A} r_i Y_{10} = \sum_{i=1}^{A} z_i. \qquad (7)$$

The system of Eqs. (5) and (6) is solved numerically for each set of deformations by expanding the single particle states onto an axial harmonic oscillator (HO) basis. For small elongation, $0 < q_{20} \leqslant 190$ b, one-center bases with $N = 14$ major shells have been considered, whereas for well-elongated configurations $q_{20} > 190$ b, two-center bases with $N = 11$ for each displaced HO basis have been used. Because calculations are performed in an even-even nucleus for which $K = 0$ (with K the projection of the spin onto the symmetry axis), the HFB nuclear states are even under time-reversal symmetry $\hat{T}$. Furthermore, we restrict the Bogoliubov space by imposing the self-consistent symmetry $\hat{T}\hat{\Pi}_2$, where $\hat{\Pi}_2$ is the reflection with respect to the xOz plane. Let us mention that the octupole operator breaks the parity symmetry. However, since $\hat{P}\hat{Q}_{30}\hat{P}^{-1} = -\hat{Q}_{30}$ and $\hat{P}\hat{H}\hat{P} = \hat{H}$ with $\hat{P}$ the parity operator, constrained HFB calculations can be restricted to positive values of q_{30}, and negative ones are obtained from $|\phi(q_{20}, -q_{30})\rangle = \hat{P}|\phi(q_{20}, q_{30})\rangle$.

The nucleus time-dependent state is defined as a linear combination of the basis states $|\phi(q_{20}, q_{30})\rangle$

$$|\Psi(t)\rangle = \int\int dq_{20}\, dq_{30}\; f(q_{20}, q_{30}, t)\,|\phi(q_{20}, q_{30})\rangle, \qquad (8)$$

where $f(q_{20}, q_{30}, t)$ is a time-dependent weight function obtained by applying the variational principle

$$\frac{\delta}{\delta f^*(q_{20}, q_{30}, t)} \int_{t_1}^{t_2} \langle\Psi(t)|\hat{H} - i\hbar\frac{\delta}{\delta t}|\Psi(t)\rangle\, dt = 0, \qquad (9)$$

where $\hat{H}$ is the same microscopic Hamiltonian as the one introduced in Eq. (5). The result is the well-known Hill-Wheeler equation which reduces to a time-dependent Schrödinger equation when the GCM problem is solved using the Gaussian overlap approximation (GOA) [16]:

$$\hat{H}_{\rm coll}\, g(q_{20}, q_{30}, t) = \; i\hbar\; \frac{\partial g(q_{20}, q_{30}, t)}{\partial t}. \qquad (10)$$

The collective wave functions $g(q_{20}, q_{30}, t)$, solutions of Eq. (10), are related to the weight functions $f(q_{20}, q_{30}, t)$ through the relation

$$g(q_{20}, q_{30}, t) = \int\int dq'_{20} dq'_{30} f(q'_{20}, q'_{30}, t) \times I^{\frac{1}{2}}(q_{20}, q_{30}, q'_{20}, q'_{30}), \qquad (11)$$

where $I^{\frac{1}{2}}(q_{20}, q_{30}, q'_{20}, q'_{30})$ is the square root kernel of the overlap kernel

$$I(q_{20}, q_{30}, q'_{20}, q'_{30}) = \langle\phi(q_{20}, q_{30})|\phi(q'_{20}, q'_{30})\rangle.$$

The exact form of the collective Hamiltonian $\hat{H}_{\rm coll}$ deduced from the GOA can be found in [14,15]. In the present derivation of this Hamiltonian, the widths G_{22}, G_{23}, and G_{33} of the Gaussian overlap between differently deformed constrained HFB states have been assumed to be constant. Numerical calculation of these widths shows that they vary very slowly in the whole q_{20}-q_{30} domain considered here and that their variations can be neglected. With this assumption, the two-dimensional collective Hamiltonian reads

$$\hat{H}_{\rm coll} = -\frac{\hbar^2}{2}\sum_{i,j=2}^{3}\frac{\partial}{\partial q_{i0}} B_{ij}(q_{20}, q_{30})\frac{\partial}{\partial q_{j0}} + V(q_{20}, q_{30}) - \sum_{i,j=2}^{3}\Delta V_{ij}(q_{20}, q_{30}), \qquad (12)$$

where $V(q_{20}, q_{30})$ is the constrained HFB deformation energy, $\Delta V_{ij}(q_{20}, q_{30})$ are the so-called zero-point-energy corrections, and $B_{ij}(q_{20}, q_{30})$ is the inverse of the inertia tensor $\mathcal{M}_{ij}(q_{20}, q_{30})$ associated with the quadrupole and octupole modes. In this work, we have taken for $\mathcal{M}_{ij}$, instead of the GCM + GOA inertia tensor, the one deduced from the adiabatic time-dependent Hartree-Fock (ATDHF) theory with the Inglis-Belyaev approximation. The reason for this replacement is that the ATDHF theory appears to give a better account of the nuclear collective inertia than does the GCM theory. This question has been extensively discussed in the literature (see, e.g., [16] and references therein).

The element ij of the Inglis-Belyaev inertia tensor can be expressed as

$$\mathcal{M}_{ij} = \sum_{k,l=2,3} (M^{(-1)})^{-1}_{ik}(M^{(-3)})_{kl}(M^{(-1)})^{-1}_{lj}. \qquad (13)$$

In Eq. (13) the moments of order $-k$ are calculated as

$$M^{(-k)}_{ij} = \sum_{\mu\nu}\frac{\langle\phi(q_{20}, q_{30})|\hat{Q}_{i0}|\mu\nu\rangle\langle\mu\nu|\hat{Q}_{j0}|\phi(q_{20}, q_{30})\rangle}{(E_\mu + E_\nu)^k}, \qquad (14)$$

where $|\mu\nu\rangle$ are two quasiparticle states with energies $E_\mu + E_\nu$ built on $|\phi(q_{20}, q_{30})\rangle$, and $\hat{Q}_{i0}$ the quadrupole/octupole deformation operator defined in Eqs. (1) and (2), respectively.

Let us mention that the collective Hamiltonian $\hat{H}_{\rm coll}$ in Eq. (12) is Hermitian because (i) all inertia are real, and (ii) $B_{23} = B_{32}$.

In addition, from Eq. (9), we find that the collective Hamiltonian and the overlap kernel are even under the change of q_{30} into $-q_{30}$. Hence, Eq. (10) propagates the collective wave function $g(q_{20}, q_{30}, t)$ without mixing parity components. In particular, if the initial wave function $g(q_{20}, q_{30}, t = 0)$ has a good parity π, the full time-dependent state Eq. (11) will be an eigenstate of $\hat{P}$ with eigenvalue π.

It is important to emphasize at this stage that the approach presented here requires only the use of an effective force. We recall that the interaction D1S permits us to employ the full HFB theory and consequently to treat the mean field and the pairing correlations on the same footing at each deformation. Also, the collective Hamiltonian $\hat{H}_{\rm coll}$, as derived from the GCM procedure, is fully microscopic and relies exclusively on the interaction D1S. Finally, let us also add that the original D1S force is used, which means that no readjustment of the parameters has been made for the application reported in this paper.

The collective Hamiltonian extracted with our procedure looks like those employed in phenomenological approaches. However, the form used in the present work directly follows from the TDGCM theory and the GOA ansatz. We emphasize that the 2×2 inertia tensor depends on the coordinates and is nondiagonal. Since this situation has not been much studied, the numerical methods used to solve Eq. (10) are presented in Sec. III. They differ from the ones previously discussed in Ref. [10] because of, first the large domain of deformation considered here, and second the symmetries of the constraints, which lead to numerical uncertainties when implementing the previously-used procedures.

III. NUMERICAL METHODS

A. Discretization of the collective variables

To preserve the Hermiticity of the collective Hamiltonian, the discretization of the collective variables has been performed by expressing the double integral of the function as

$$F(t) = \int\int dq_{20}\, dq_{30}\; g^*(q_{20}, q_{30}, t) \times \left(\hat{H}_{\rm coll} - i\hbar\,\frac{\partial}{\partial t}\right) g(q_{20}, q_{30}, t), \qquad (15)$$

with finite differences

$$F(t) = \sum_{ik,jl} g^*(i,k,t)\ K_{ik,jl}\ g(j,l,t), \tag{16}$$

and by deriving the discretized equation from the variational principle,

$$\frac{\partial F(t)}{\partial g^*(i,k,t)} = 0. \tag{17}$$

In Eq. (16), K is the symmetric matrix representing $\hat{H}_{\rm coll}$ (whose full expression is given in Appendix A), and the labels ik and jl correspond to the q_{20} and q_{30} variables through $q_{20}(i) = (i-1)\Delta q_{20}$, and $q_{30}(k) = (k-1)\Delta q_{30}$.

The time-dependent GCM + GOA equation becomes

$$\sum_{jl} K_{ik,jl}\ g(j,l,t) = \ i\hbar\ \frac{\partial}{\partial t}\ g(i,k,t). \tag{18}$$

In practice, the two-dimensional discretized form Eq. (18) has been reduced to a one-dimensional problem by defining a linear index $m = l + (k-1) \times l_{\max}$, with $l_{\max}$ the largest value of l on the grid, which yields

$$\sum_{m} K_{nm} g_m(t) = \ i\hbar\ \frac{\partial}{\partial t} g_n(t). \tag{19}$$

The resulting 2×2 discretized Hamiltonian matrix H_{mn} is symmetric, and the Hermitian character of the kinetic energy operator is preserved. From a numerical point of view, H_{mn} is a sparse matrix. The corresponding nonzero elements are stored using the "row-indexed storage" method [17], an efficient technique for reducing computing times.

B. Time evolution

In matrix form, the evolution of g between t and $t + \Delta t$ can be written

$$g(t + \Delta t) = e^{-i\frac{K\Delta t}{\hbar}}\ g(t). \tag{20}$$

Using the Crank-Nicholson method [17,18], a unitary and stable algorithm, Eq. (20) becomes

$$G(t + \Delta t) = \frac{1 - i\frac{K\Delta t}{2\hbar}}{1 + i\frac{K\Delta t}{2\hbar}}\ G(t) + O[(K\Delta t)^3]. \tag{21}$$

This equation can be transformed into the linear system:

$$\left(1 + i\frac{K\Delta t}{2\hbar}\right)\ g(t + \Delta t) = \left(1 - i\frac{K\Delta t}{2\hbar}\right) g(t). \tag{22}$$

In this study, Eq. (22) is solved by successive iterations until convergence. The wave function $g(t + \Delta t)$ at time $t + \Delta t$ is determined from the previously known wave function $g(t)$ at time t as follows:

$$\begin{cases} g^{(n=0)}(t + \Delta t) = g(t) \\ g^{(n+1)}(t + \Delta t) = \left(1 - i\dfrac{K\Delta t}{2\hbar}\right) g(t) \\ \qquad\qquad - i\dfrac{K\Delta t}{2\hbar} g^{(n)}(t + \Delta t). \end{cases} \tag{23}$$

Equations (23) are solved in a q_{20}-q_{30} box of finite extension assuming $g(q_{20}, q_{30}, t) = 0$ along the edges of the box. This boundary condition leads to unphysical reflections of the time-dependent wave function on the $q_{20} = q_{20\max}$ edge of the box. To eliminate these unphysical reflections, the same technique as that detailed in Ref. [13] has been implemented: The wave function is progressively absorbed in the interior of a rectangular region $q'_{20\max} \leqslant q_{20} \leqslant q''_{20\max}$ beyond the $q_{20} = q_{20\max}$ edge (in the present work $q_{20\max} = 550$ b, $q'_{20\max} = 800$ b, and $q''_{20\max} = 1300$ b). Inside this region, the wave function $g(t)$ is multiplied at each time-step Δt by the function of Woods-Saxon structure:

$$F(q_{20}) = \frac{1}{1 + \exp[-0.015(q_{20} - 1150)]}. \tag{24}$$

As mentioned in Ref. [13], this technique is similar to adding an imaginary potential $-i\hbar F(q_{20})/\Delta t$ beyond the boundary $q_{20} = q'_{20\max}$. Since Δt occurs in this imaginary potential, $F(q_{20})$ is optimized for each time step. In the present study, the numerical values in Eq. (24) have been optimized to avoid reflections for a time-step $\Delta t = 1.3 \times 10^{-24}$ s.

The initial wave function $g(t = 0)$ is described in terms of quasistationary vibrational states localized in the first well of the potential energy surface. The states in question are in fact taken as the eigenstates of a modified two-dimensional q_{20}-q_{30} potential, where the first fission barrier is extrapolated to large positive values as mentioned in Ref. [19]. Only the states lying between the top of the inner barrier and 2 MeV above have been considered in the present work.

Fragment mass distributions $Y(A_H)$ are derived by a time-integration of the flux $\vec{J}(q_{20}, q_{30}, t) \cdot \vec{n} ds$ of the wave function through scission at a given fragmentation,

$$Y(A_H) = \int_0^T dt\ \vec{J}(q_{20}, q_{30}, t) \cdot \vec{n} ds, \tag{25}$$

where T is the time for which the time-dependent flux is stabilized along the scission line. In Eq. (25), $\vec{n}$ is a vector normal to the scission line, and $\vec{J}$ is the current defined from the continuity equation

$$\frac{d}{dt}|g(q_{20}, q_{30}, t)|^2 = -\mathrm{div}\vec{J}(q_{20}, q_{30}, t). \tag{26}$$

The current $\vec{J} = (J_2, J_3)$ as calculated with the collective Hamiltonian defined in Eq. (12) takes the form

$$\begin{aligned} J_2(q_{20}, q_{30}, t) = \frac{\hbar}{2i}\Bigg(& g^* B_{22}\frac{\partial g}{\partial q_{20}} - g B_{22}\frac{\partial g^*}{\partial q_{20}} \\ & + g^* B_{23}\frac{\partial g}{\partial q_{30}} - g B_{23}\frac{\partial g^*}{\partial q_{30}}\Bigg), \\ J_3(q_{20}, q_{30}, t) = \frac{\hbar}{2i}\Bigg(& g^* B_{33}\frac{\partial g}{\partial q_{30}} - g B_{33}\frac{\partial g^*}{\partial q_{30}} \\ & + g^* B_{32}\frac{\partial g}{\partial q_{20}} - g B_{32}\frac{\partial g^*}{\partial q_{20}}\Bigg). \end{aligned} \tag{27}$$

Expression (27) reveals in particular that the component of the current in one direction involves the gradients in all directions. This observation will be used in Sec. V, where we discuss the contributions of interference terms between components of different parities in the initial state.

IV. STATIC RESULTS

A. Potential energy surface

The HFB calculations have been performed for ^{238}U with constraints on both the quadrupole and octupole moments, using the mesh sizes $\Delta q_{20} = 5$–10 b and $\Delta q_{30} = 2$–4 b$^{3/2}$. The range of investigation extends from spherical shapes ($q_{20} = 0$ b) up to elongations of the exit points, which vary from $q^a_{20\max} = 320$ b for the most asymmetric fission ($q_{30} = 44$ b$^{3/2}$) up to $q^s_{20\max} = 550$ b for symmetric fragmentation ($q_{30} = 0$ b$^{3/2}$). For each value of the quadrupole moment, the HFB calculations have been restricted to solutions whose excitation energies are at most 30 MeV above the ground state. For values of q_{20} near scission, this condition leads to a maximum value of $q_{30} = 120$ b$^{3/2}$. HFB solutions for $120 < q_{30} < 200$ b$^{3/2}$ have been extrapolated.

Figure 1 shows the most significant part of the HFB potential energy surface as a function of the quadrupole and octupole moments. For practical reasons, the domain of the plot is restricted to $0 < q_{20} < 320$ b and $0 < q_{30} < 72$ b$^{3/2}$ and energies are truncated to 25 MeV. As expected in this actinide nucleus, the ground state is deformed with $q_{20} \approx 30$ b and a super-deformed minimum appears for an elongation close to $q_{20} = 80$ b. Beyond this second well, two valleys appear. They are separated by a ridge for well-elongated shapes and lead to either the symmetric or the most probable asymmetric fragmentations.

For each asymmetry, the determination of scission configurations is made by increasing the elongation step by step: the constrained HFB wave function at a given q_{20} is generated from a previous solution at a slightly lower elongation while keeping q_{30} fixed. This method relies on the scission mechanism studied in [10]. It is assumed that scission occurs for a given value of q_{30} when the system falls from the so-called fission valley to the fusion valley describing well-separated fragments.

The main criterion used to define exit points and to separate pre- and post-scission configurations is obtained by looking at the nucleon density in the neck. We consider that the system is composed of two fragments when the density in the neck

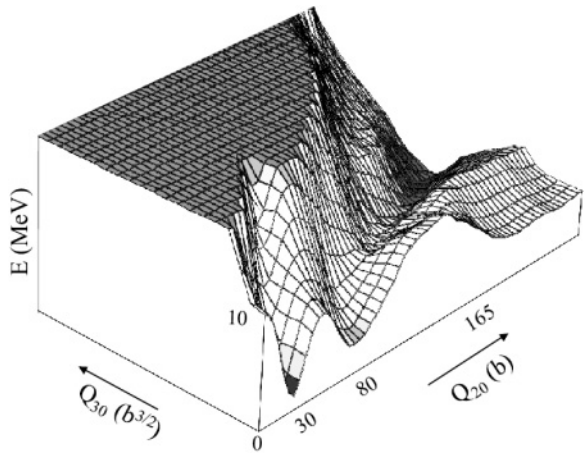

FIG. 1. HFB potential energy surface as a function of q_{20} and q_{30} collective variables in ^{238}U.

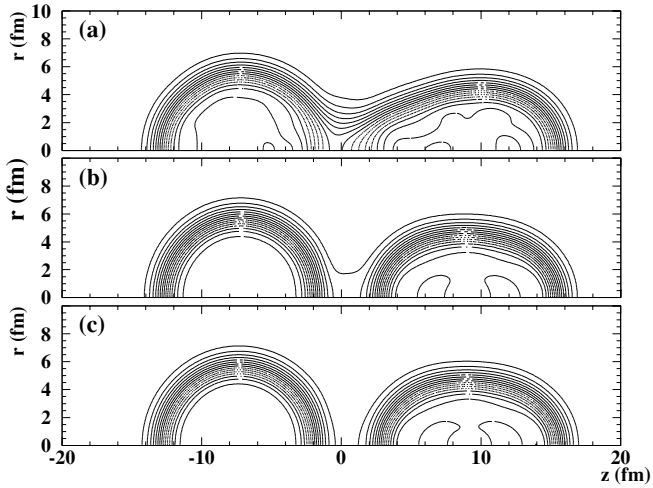

FIG. 2. Proton plus neutron density contours at a given asymmetry $q_{30} = 44$ b$^{3/2}$ for different elongations (a) $q_{20} = 310$ b, (b) $q_{20} = 320$ b, and (c) $q_{20} = 330$ b. Contour lines are separated by 0.01 nucleons/fm^3.

is less than 0.01 nucleon/fm^3. This is illustrated in Fig. 2, where density contours are plotted for a given asymmetry $q_{30} = 44$ b$^{3/2}$ and an increasing elongation. Contour lines are separated by 0.01 nucleon/fm^3. Figures 2(a) and 2(b) correspond to pre-scission configurations and Fig. 2(c) to a post-scission one. Let us note that the two criteria described in Ref. [10] are also satisfied: a $\simeq$15-MeV drop in the energy of the total system and a $\simeq$30% decrease of the hexadecapole moment are observed when scission occurs.

It is worth pointing out that the constrained HFB method does not impose an *a priori* shape to the fissioning system. All types of deformations that are not imposed take the values that minimize the total nuclear energy with both the nuclear mean field and the pairing field determined self-consistently. Results concerning fragment deformations at scission will be presented in a forthcoming publication.

Near the exit points, the z location of the neck $z_{\rm neck}$ is determined as the z value for which the nucleon density integrated over r is minimum. Properties of the fragments such as their masses, charges, and deformations, and the distance between their centers of charge are calculated from integrations in the left and right half-spaces on either side of the $z = z_{\rm neck}$ plane. As an example, the distance d between the centers of charge of the fragments is plotted in Fig. 3 as a function of the heavy fragment mass. It is maximum for $A_H = 119$ with $d = 20.27$ fm and minimum for $A_H = 134$ with $d = 15.88$ fm. Precise values of this fragment center of charge distance are crucial because they govern the total kinetic energy (TKE) distribution, as discussed in Sec. IV C. As a test, we have checked that the analytical relations in Eq. (3) are fulfilled.

B. Pairing correlations

Figure 4 shows the pairing energy $E_{\rm pair} = \frac{1}{2}{\rm Tr}(\Delta\kappa)$, where Δ and κ are the pairing field and the pairing tensor, respectively. We clearly see that pairing is not constant as a

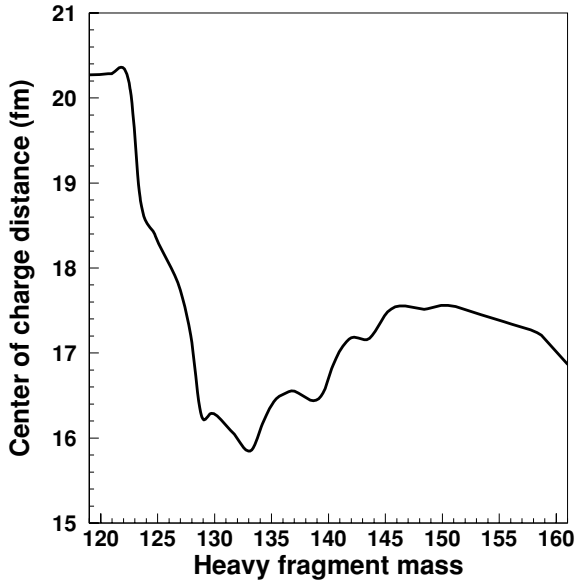

FIG. 3. Distance between the centers of charge of the fragments as a function of the heavy fragment mass.

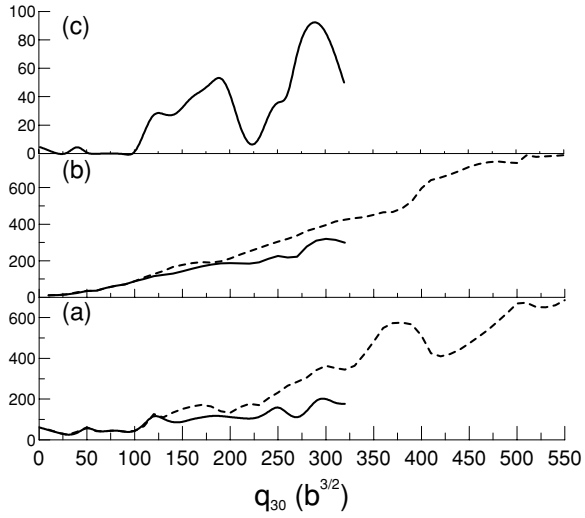

FIG. 5. Components of the inertia tensor (a) B_{22} (in MeV $b^2\hbar^2$), (b) B_{33} (in MeV $b^3\hbar^2$), and (c) B_{23} (in MeV $b^{5/2}\hbar^2$) as functions of q_{20} along the asymmetric (solid line) and the symmetric (dashed line) fission paths.

function of elongation. As expected, minima are found inside the wells and maxima at the top of barriers. Furthermore, the total pairing energy E_{pair} is predicted to be lowest in the asymmetric valley ($E_{\text{pair}} \approx 6$ MeV) and much larger in the symmetric one ($E_{\text{pair}} > 15$ MeV). These variations of the pairing correlations are very important because they strongly influence both the collective flux and the occurrence of intrinsic excitations, as is now explained.

First, the collective inertia is known to be very sensitive to pairing correlations. The three components B_{22}, B_{33}, and B_{23} of the inertia tensor in Eq. (12) are plotted in Figs. 5(a), 5(b), and 5(c), respectively, as functions of the elongation along the symmetric (dotted line) and asymmetric (solid line) paths. The two components B_{22} and B_{33} are larger in the symmetric valley than in the asymmetric one (up to a factor of 2 at large elongation). Furthermore, whereas the nondiagonal inertia component B_{23} is zero for $q_{30} = 0$ by definition, B_{23} is found to be non-negligible as soon as the system spreads widely in the asymmetric valley. The coupling brought by B_{23} between the q_{20} and q_{30} modes indicates that as time evolves, the two collective degrees of freedom exchange energy, which will affect, among other things, the kinetics of the fission process.

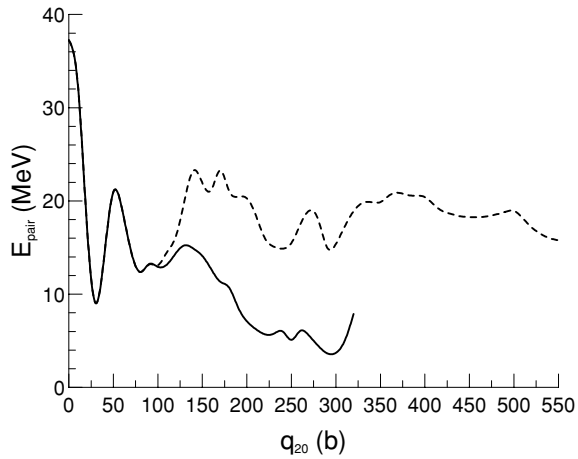

FIG. 4. Pairing energy as a function of q_{20} along the asymmetric (solid line) and the symmetric (dashed line) fission paths in ^{238}U.

Second, pairing correlations characterize the amount of superfluidity of the collective flux and the onset of dissipation, particularly between the saddle point and the exit point. In the HFB approach, dissipation requires the creation of two quasiparticle excitations, which is a transfer of energy from the collective motion at least equal to 2Δ, where Δ is the energy necessary to break a correlated pair. One expects that small values of Δ will favor dissipation. However, the excitation of the intrinsic structure also depends on the coupling between collective and intrinsic degrees of freedom, which is largely unknown. For this reason, the question of dissipation effects will be addressed in future work. The proton and neutron gaps $2\Delta_p$, $2\Delta_n$ are plotted in Fig. 6 as functions of elongation along the asymmetric path. The corresponding potential energy curve is also plotted (dotted curve) to guide the eye. For proton pairing correlations, we find $2\Delta_p = 2.3$ MeV at the top of the second barrier. This value appears to be in good agreement with experimental data [20–22]. As a matter of fact, manifestations of proton pair breaking are observed in ^{238}U and ^{239}U nuclei for an excitation energy of 2.3 MeV above the barrier: first the proton odd-even effect observed in the fragment mass distributions decreases exponentially for an excitation energy slightly higher than 2.3 MeV [20] and then the total kinetic energy drops suddenly [21,22].

In Fig. 6 we also see that the proton gap decreases rapidly during the first part of the descent beyond the saddle point; for instance, $2\Delta_p = 1.4$ MeV for $q_{20} = 180$ b. However, experimental facts show that increasing the excitation energy from 0 to 2.2 MeV above the barrier does not modify the

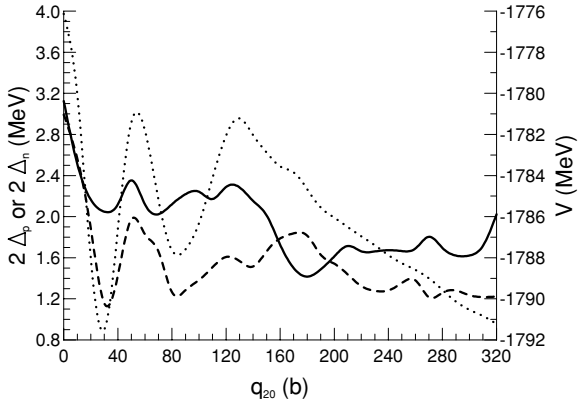

FIG. 6. Twice the proton (solid curve) and neutron (dashed curve) lowest quasiparticle energies and potential energy (dotted curve) along the asymmetric path as functions of the elongation in barns.

proton odd-even effect. From our point of view, this could be an indication that no proton pairs are broken during the descent from saddle to scission in low-energy fission for excitation energies below 2.2 MeV above the barrier. Our interpretation is that the excitation energy supplied during the descent is shared among the collective degrees of freedom and not among intrinsic excitations. This experimental observation gives us some confidence that the neglect of the coupling between collective and intrinsic degrees of freedom is a reasonable approximation to start with in low-energy fission.

Finally, no strong odd-even neutron effects are observed for the fragment mass distributions measured in the photofission of ^{238}U, regardless of excitation energy [21]. In our calculations, the neutron pairing gap is much lower than the proton one, except for $160 < q_{20} < 190$ b, as displayed in Fig. 6. At the top of the second barrier, the neutron gap is only $2\Delta_n = 1.6$ MeV. This tends to indicate that neutron pairs are more likely to be broken than proton ones in the even-even ^{238}U nucleus at low excitation energy. But no definite comparison with experimental data can be made since a precise knowledge of the neutron number of the fission fragments is made extremely difficult by the neutron evaporation. All these remarks concerning pairing correlations *a posteriori* illustrate the fact that pairing correlations play an essential role and that they should be introduced in dynamical studies of fission.

C. Total kinetic energy distribution

As a first estimate, the total kinetic energy TKE of the fragments can be roughly calculated as the Coulomb potential energy $E_K = \frac{Z_H Z_L e^2}{d}$, with d the distance between the centers of charge of the fragments at scission. Theoretical values calculated along the scission line are shown in Fig. 7 as a function of A_H, the heavy fragment mass. They are compared to experimental data obtained from the photofission of ^{238}U using 6.2 MeV bremsstrahlung γ rays, corresponding to an excitation energy close to the inner fission barrier height [21]. We first notice that the general trend of the distribution is rather well reproduced, with a dip at $A_H = 119$ and a peak at

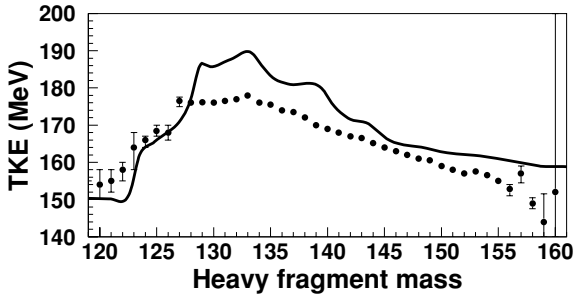

FIG. 7. Total kinetic energy distributions as functions of the heavy fragment mass. Dots indicate experimental data [21], and the continuous line represents predictions.

$A_H = 134$. Symmetric and asymmetric wings are surprisingly close to experimental data. The agreement indicates that our microscopic approach, together with the prescription explained in Sec. IV A, is able to give a realistic description of scission configurations. The main difference with experimental data occurs in the region of the most probable asymmetric fission where the theoretical results overestimate TKE values by $\simeq$6%. This discrepancy mainly comes from the fact that the nuclear contribution entering the mutual energy between the two fragments is not strictly zero for the corresponding scission configurations. Furthermore, the attractive exchange Coulomb energy between the fragments has been neglected. These two effects could lead to a decrease of TKE values that may reach 10–15 MeV.

D. "One-dimensional" fragment mass distribution

As a first approximation, mass distributions can be derived using the fragmentation model detailed in Ref. [23]. Namely, collective stationary vibrations are studied along the sole mass-asymmetry degree of freedom for nuclear configurations just before scission. The probability of occurrence of a mass asymmetry (A_H, A_L) corresponding to a value q_{30} of the octupole moment is then taken as

$$Y(A_H, A_L) = \left|\Psi_0^{+1}(q_{30})\right|^2, \tag{28}$$

where Ψ_0^{+1} is the positive parity eigenstate with the lowest energy of the one-dimension collective Hamiltonian $\hat{H}'_{\rm coll}$ in the q_{30} variable,

$$\hat{H}'_{\rm coll}\left(q_{30}, \frac{\partial}{\partial q_{30}}\right) = -\frac{\hbar^2}{2}\frac{\partial}{\partial q_{30}}\frac{1}{\mathcal{M}_3(q_{30})}\frac{\partial}{\partial q_{30}} + V(q_{30}) - \Delta V_3(q_{30}). \tag{29}$$

Here, $V(q_{30})$ is the HFB deformation energy along the scission line $q_{20} = q_{20}^s = f(q_{30})$, $\mathcal{M}_3(q_{30})$ is the collective inertia, and $\Delta V_3(q_{30})$ is the zero-point-energy (ZPE) correction. The Hamiltonian of Eq. (29) is derived from the usual GOA reduction of the one-dimensional Hill-Wheeler stationary equation obtained by taking for the generator coordinate the curvilinear abscissa $s(q_{20}, q_{30})$ along the scission line. A change of variable is then performed in order to express all quantities as functions of q_{30}. It is easy to show that the inertia and ZPE correction appearing in Eq. (29) are related to those

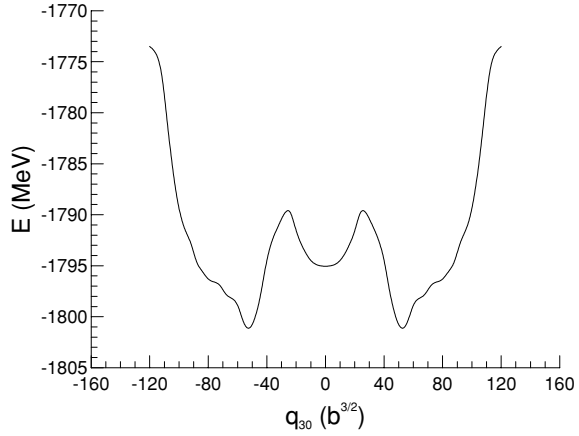

FIG. 8. Potential energy along the scission line as a function of the octupole moment.

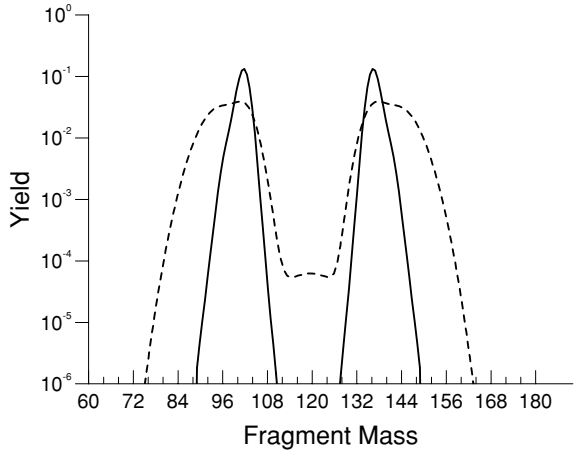

FIG. 9. Comparison between the one-dimensional mass fragment distribution obtained from (28) (solid line) and the Wahl evaluation (dashed line) [24].

entering the full two-dimensional Hamiltonian (12); that is,

$$\mathcal{M}_3(q_{30}) = \left(\frac{df}{dq_{30}}\right)^2 M_{22} + 2\left(\frac{df}{dq_{30}}\right) M_{23} + M_{33}, \qquad (30)$$

$$\Delta V_3(q_{30}) = \frac{\mathcal{G}_3(q_{30})}{2\mathcal{M}_3(q_{30})}, \qquad (31)$$

with

$$\mathcal{G}_3(q_{30}) = \left(\frac{df}{dq_{30}}\right)^2 G_{22} + 2\left(\frac{df}{dq_{30}}\right) G_{23} + G_{33}, \qquad (32)$$

where $\mathcal{M}_{ij}$ are the inertia defined in Eq. (13) and G_{ij} the components of the overlap tensor calculated in the cranking approximation using the moments of Eq. (14).

Clearly, the model based on the Hamiltonian (29) ignores all the effects of the dynamics along the elongation degree of freedom from the first well to scission. We call the mass distribution obtained in this way a "one-dimensional" mass distribution.

The HFB potential energy $V(q_{30})$ calculated along the scission line is plotted in Fig. 8 as a function of the octupole moment. The lowest energy is obtained for $q_{30} = \pm 44$ b, corresponding to the most probable fission. A secondary minimum is found for $q_{30} = 0$ b. These two wells are separated by an 11-MeV-high barrier.

One-dimensional distributions are shown in Fig. 9 where the mass yield Eq. (28) is plotted (solid line) together with the Wahl evaluation (dashed line) for 46 keV neutron-induced fission on ^{237}U [24]. The maxima of the theoretical curve occur at $A_H = 134$, $A_L = 94$ values corresponding to the minima of the potential energy along the scission line. The fact that the experimental curve maxima lie close to these values indicates that the most probable fragmentation is due essentially to the properties of the potential energy surface at scission, i.e., mainly to shell effects in the nascent fragments. However, the one-dimensional approach does not reproduce either the experimental peak-to-valley ratio or the experimental widths of the distributions—the theoretical widths are two times smaller than the Wahl evaluated ones.

One must note, however, that only the solution of Eq. (29) with lowest energy Ψ_0^{+1} has so far been considered. This is certainly an oversimplifying assumption since the wave function describing the collective evolution of the nucleus will undoubtedly possess a more complicated structure at the time of reaching the scission line. In particular, as mentioned in Ref. [25], for $n > 0$ states Ψ_n^π, solutions of Eq. (29) may become excited because of the interaction between q_{20} and q_{30} degrees of freedom. Let us mention that in Ref. [25] the population of the eigenstates was assumed to follow a Boltzmann law governed by a temperature parameter. In Ref. [26], the elongation degree of freedom was introduced using a classical approximation.

Amplitudes of the first six collective states $\Psi_n^\pi, n = 0, \ldots, 5$, solutions of Eq. (29) are displayed in Fig. 10 as functions of the fragment mass. As is well known, such Ψ_n^π states are eigenstates of the parity operator Π with eigenvalues π. Positive and negative parity states are plotted in solid and dotted lines, respectively. Each pair of $\pi = +1$ and $\pi = -1$ levels is degenerate in energy because the potential is symmetric with respect to the $q_{30} \to -q_{30}$ transformation and because the barrier between the two asymmetric wells is high (11 MeV) (see Fig. 8). We observe in Fig. 10 that the excited states are more spread over mass than is the ground state. For example, the wave functions Ψ_4^{+1} and Ψ_5^{-1} displayed in Fig. 10(c) display nonzero values up to $A_H \approx 156$, whereas the lowest energy wave functions Ψ_0^{+1} and Ψ_1^{-1} in Fig. 10(a) are localized in the domain $132 < A_H < 144$. Therefore, we can expect that the introduction of these excited states in the definition of the mass yield Eq. (28) will broaden the mass distribution in the asymmetric region.

V. DYNAMIC RESULTS

A. Initial states

The time-dependent evolution of the system has been calculated using different initial conditions in the first well of the potential energy surface. Calculations have been performed

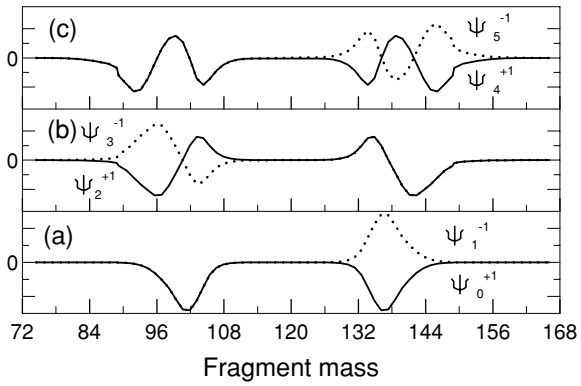

FIG. 10. Amplitudes of the first six collective states in the asymmetry variable at scission as functions of the fragment mass. Positive (negative) parity states are plotted in solid (dotted) lines. Excitation energies, measured from the lowest energy state, are (a) $E = 0$ MeV, (b) $E = 3.09$ MeV, and (c) $E = 4.76$ MeV.

from $t = 0$ up to maximum times for which the flux of the time-dependent collective wave function along the scission line has become stabilized.

We first discuss the effect of the structure of the initial state on the mass distribution. To define the initial conditions, we imagine that the nucleus is a compound system described in terms of complicated quasistationary states that decay into various channels (neutron and γ-ray emission and fission). In the case of the even-even $K = 0$ ^{238}U nucleus studied here, we assume that states which decay through fission can be described by the simple form

$$|\Psi_{P,K=0,I,M}\rangle = (2\pi)^{-\frac{1}{2}} Y_I^M(\Omega) \int dq \; f_n^\pi(q, t = 0) \; |\phi(q)\rangle, \tag{33}$$

where $Y_I^M(\Omega)$ are spherical harmonics and Ω the Euler angles relating the intrinsic axes of the nucleus to the laboratory frame of reference.

The parity quantum number P is related to the intrinsic parity π by the following relation:

$$P = \pi(-1)^I, \tag{34}$$

where I is the spin of the fissioning system. In Eq. (33), q is the set of all relevant nuclear collective deformations which in the present work [see Eq. (8)] is restricted to (q_{20}, q_{30}).

As already mentioned in Sec. II, initial states $g_n^\pi(q_{20}, q_{30}, t = 0)$ [related to the $f_n^\pi(q_{20}, q_{30}, t = 0)$ functions as in Eq. (11)] are taken as eigenstates of the modified two-dimensional first well $V'(q_{20}, q_{30})$, where the potential has been extrapolated at large deformations as shown in Fig. 11. They are solutions of the equation

$$\hat{H}'_{\rm coll} \; g_n^\pi(q_{20}, q_{30}, t = 0) = E_n^\pi \; g_n^\pi(q_{20}, q_{30}, t = 0), \tag{35}$$

where $\hat{H}'_{\rm coll}$ is the Hamiltonian defined in Eq. (12) with $V(q_{20}, q_{30})$ replaced by $V'(q_{20}, q_{30})$.

Because $H'_{\rm coll}(q_{20}, q_{30}, \frac{\partial}{\partial q_{20}}, \frac{\partial}{\partial q_{30}}) = H'_{\rm coll}(q_{20}, -q_{30}, \frac{\partial}{\partial q_{20}}, -\frac{\partial}{\partial q_{30}})$, these initial states can be chosen as eigenstates of the parity operator with eigenvalues $\pi = \pm 1$ [27]:

$$g_n^\pi(q_{20}, -q_{30}, t = 0) = \pi \; g_n^\pi(q_{20}, q_{30}, t = 0). \tag{36}$$

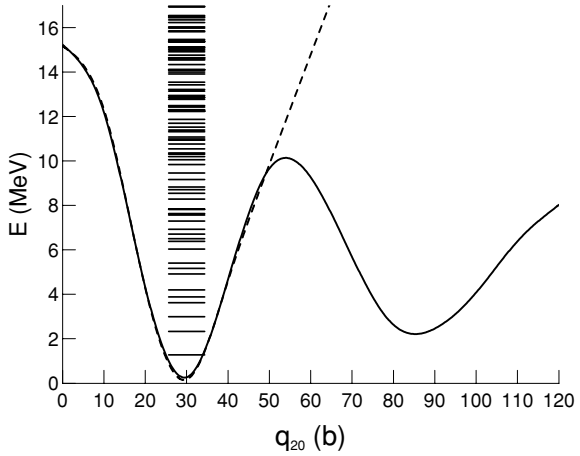

FIG. 11. Potential curves $V(q_{20}, q_{30} = 0)$ and $V'(q_{20}, q_{30} = 0)$ including zero-point-energy corrections (continuous and dotted lines, respectively), and collective eigenstates of the modified $V'(q_{20}, q_{30} = 0)$ potential (horizontal segments).

The potential curves $V(q_{20}, q_{30} = 0)$ and $V'(q_{20}, q_{30} = 0)$ including zero-point-energy corrections are displayed in Fig. 11. The eigenenergies of $H'_{\rm coll}$ are also shown. Excitation energies of the compound nucleus in the interval $[B_I, B_I + 2.5$ MeV] will be considered in this work focusing on low-energy fission, where B_I is the first barrier height. In this energy range, the mean level spacing is around 130 keV. Therefore, 19 states are possible initial candidates for our dynamic calculations. All these states are located above the outer symmetric saddle point but below the outer asymmetric one. They correspond to multiple quadrupole and octupole phonons and have different components along the q_{30} and q_{20} directions. Significant effects on the fragment mass distributions are mainly due to the parity of the initial states.

In Fig. 12, fragment mass distributions calculated with formula (25) for initial states of definite parity are plotted separately. The solid and dotted curves correspond to initial states whose intrinsic parity is exclusively positive or negative. They are located at 2.4 and 2.3 MeV above the first barrier, respectively.

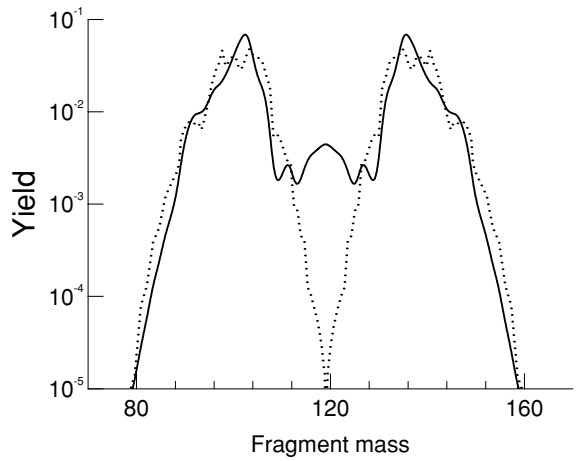

FIG. 12. Fragment mass distributions obtained for initial states having positive parity (solid line) and negative parity (dotted line).

We see that the main difference between the two results is the peak-to-valley ratio, which is near 50 for the positive parity initial state and infinite for the negative one. The fact that no symmetric fission is found when the initial state has a negative parity is because $g_n^{-1}(q_{20}, q_{30} = 0, t) = 0$ if $\pi = -1$ for any time t. As a consequence, the flux of the wave function through the scission line at $q_{30} = 0$ vanishes.

In the applications presented below we use initial states that do not have a definite parity. As we observed at the end of Sec. III, there are interferences between states of different parities in the calculation of the flux. However, because of the symmetries of the inertia tensor, these interferences do not contribute to the symmetric mass fragmentation. From the previous discussion, we infer that our predictions of symmetric fission will be affected by the proportions of collective states with negative and postive intrinsic parity. To get an estimate of these proportions, we assume that they are the same as in the compound sytem $n + {}^{237}\mathrm{U}$. More precisely, by using Eq. (34) we define fission cross sections, $\sigma(\pi = +1, E)$ and $\sigma(\pi = -1, E)$, corresponding to components of intrinsic parity in the compound system through the relations

$$\begin{aligned}\sigma(\pi = -1, E) = &\sum_{I=2p, P=-1} \sigma_{CN}(P, I, E)\ P_f(P, I, E) \\ &+ \sum_{I=2p+1, P=+1} \sigma_{CN}(P, I, E)\ P_f(P, I, E), \\ \sigma(\pi = +1, E) = &\sum_{I=2p, P=+1} \sigma_{CN}(P, I, E)\ P_f(P, I, E) \\ &+ \sum_{I=2p+1, P=-1} \sigma_{CN}(P, I, E)\ P_f(P, I, E),\end{aligned} \tag{37}$$

where E, P, $\sigma_{CN}(P, I, E)$, and $P_f(P, I, E)$ are the energy, the parity [defined in Eq. (34)], the formation cross section, and the fission probability of the compound nucleus, respectively.

Formation cross sections were calculated using the Hauser-Feschbach theory with the optical potential model of Ref. [28] and fission probabilities were deduced from a statistical model calculation [29].

Then, we define probabilities by the following fractions:

$$\begin{aligned}p^-(E) &= \frac{\sigma(\pi = -1, E)}{\sigma(\pi = -1, E) + \sigma(\pi = +1, E)}, \\ p^+(E) &= \frac{\sigma(\pi = +1, E)}{\sigma(\pi = -1, E) + \sigma(\pi = +1, E)}.\end{aligned} \tag{38}$$

They represent the population of states in the compound system that have a given intrinsic parity and decay to fission. With the help of these probabilities, we determine the mixing of parities in the initial states. Numerical values for the reaction $n + {}^{237}\mathrm{U}$ are given in Table I for two excitation energies as measured from the top of the first barrier.

Mass distributions obtained for these two energies are displayed in Fig. 13; the solid and dashed lines correspond to the two energies, 2.4 and 1.1 MeV, respectively. We observe that the symmetric fragmentation is slightly higher at excitation energy 1.1 MeV than at 2.4 MeV. Clearly, this approach does not reproduce an essential feature of measured

TABLE I. Percentages of positive and negative intrinsic parity states populated in the compound nucleus $^{238}\mathrm{U}$ by the $n + {}^{237}\mathrm{U}$ reaction for two excitation energies.

E (MeV)	1.1	2.4
$p^+(E)\,\%$	77	54
$p^-(E)\,\%$	23	46

or evaluated mass fragment distributions, namely, a sensitive increase of the symmetric fission yield with increasing neutron energy. As can be inferred from previous discussions, this discrepancy is a direct consequence of the rapid decrease with increasing energy of positive parity components in the initial state. More detailed comparisons of the theoretical predictions with Wahl evaluations [24] in Fig. 14 indicate, however, that the microscopic approach reproduces successfully various characteristics of the mass distribution.

For instance, the comparison at 2.4 MeV shows that the main features of Wahl's distribution—position and height of the maxima, peak-to-valley ratio, and broadening of the distribution—are satisfactorily reproduced by the theory. The agreement at lower energy is not as good, essentially because of the discrepancy mentioned earlier.

Initial conditions appear to be crucial for the prediction of mass distributions at low energy. In view of the quality of the results presented, we are considering studying this question more carefully in future works.

B. Dynamic effects

To analyze the influence of dynamic effects, we compare in Fig. 15 the fragment mass distribution obtained for the initial state located 2.4 MeV above the first barrier shown in Fig. 14(a) with our previous one-dimensional distribution. Fig. 15 also shows the evaluated data from the Wahl systematics (dashed curve) [24].

We first note that the maxima of the two theoretical distributions are both located around $A_H = 134$ and $A_L = 104$, in

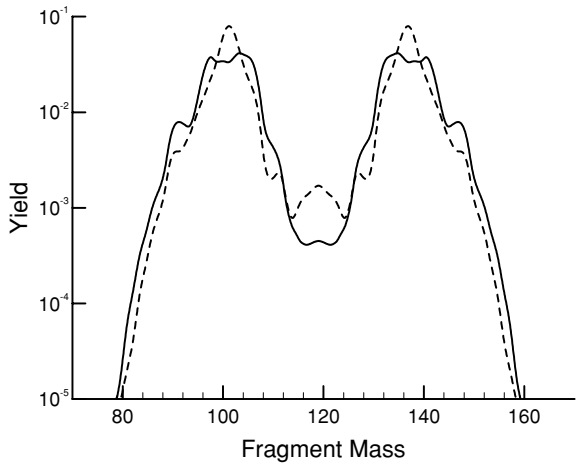

FIG. 13. Fragment mass distributions obtained for two initial states. Solid line: $E = 2.4$ MeV with $p^+ = 54\%$ and $p^- = 46\%$. Dashed line: $E = 1.1$ MeV with $p^+ = 77\%$ and $p^- = 23\%$.

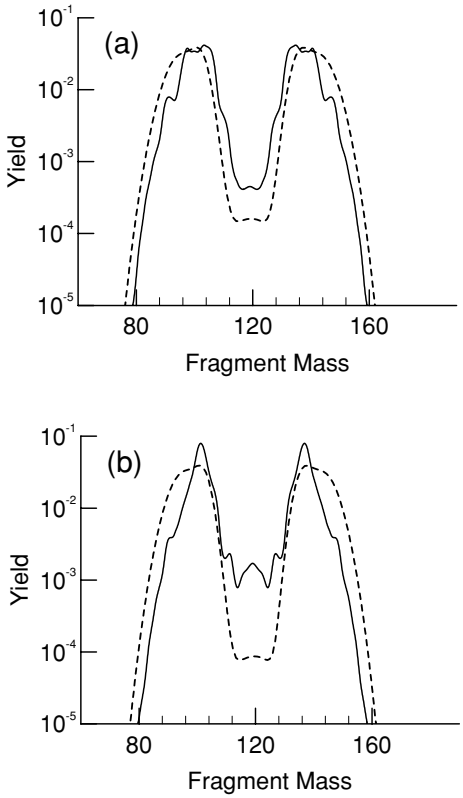

FIG. 14. Theoretical mass distributions (solid lines) are compared with the Wahl evaluations of neutron-induced fission of ^{238}U [24] (dashed lines). Excitation energies of the compound ^{238}U nucleus measured above the barrier are (a) $E = 2.4$ MeV, (b) $E = 1.1$ MeV.

good agreement with the evaluated data. As already mentioned in Sec. IV D, this is a confirmation that the most probable fragmentation is due essentially to shell effects in the nascent fragments and not to dynamic effects. The widths of the peaks obtained from the full dynamic calculation are much larger—

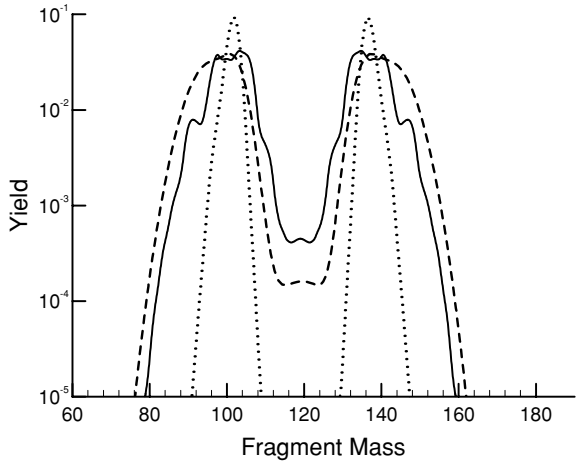

FIG. 15. Comparison between the one-dimensional mass distribution of Fig. 9 (dotted line), the mass distribution resulting from the dynamic calculation (solid line) with the initial state located 2.4 MeV above the barrier, and the Wahl evaluation (dashed line) [24].

TABLE II. Percentages of the one-dimensional states contained in the dynamic solution at scission for $t = 0.96 \times 10^{-20}$ s.

n	1–2	3–4	5–6	7–8	9–10
R_n %	35.2	8.6	36.7	6.9	12.6

about twice as large—than those of the one-dimensional case, and consequently they are in much better agreement with the Wahl evaluated data. Clearly the dynamics play a major role in the broadening of the fragment mass distributions. In the present dynamic calculation, the broadening is clearly due to the interaction between the elongation and the asymmetry degrees of freedom, which results from both the potential energy and the inertia variations. As already discussed in Sec. III, these effects are especially important in the descent from saddle to scission, where the inertia component B_{23} is large (see Fig. 5). In fact, the cross term in the kinetic energy of the collective Hamiltonian appears to be responsible for exchanges of energy between the two modes and for the spreading of the time-dependent wave function in the asymmetric valley.

To quantitatively analyze those effects, we expanded the time-dependent wave function $g(q_{20}, q_{30}, t)$ over the one-dimensional states $\Psi_n^\pi(q_{30})$ described in Sec. IV D along the line $q_{20} = (q_{20})_s = f(q_{30})$ such that

$$g[(q_{20})_s, q_{30}, t] = \sum_n C_n(t)\ \Psi_n^\pi(q_{30}). \tag{39}$$

The weight coefficients $C_n(t)$ can be calculated as

$$C_n(t) = \int dq_{30}\ g[(q_{20})_s, q_{30}, t]\ \Psi_n^\pi(q_{30}), \tag{40}$$

and the fraction of each one-dimensional state contained in the dynamic solution at scission is given by

$$R_n(t) = \frac{|C_n(t)|^2}{\sum_m |C_m(t)|^2}. \tag{41}$$

Results for $R_n(t = 0.96 \times 10^{-20}\ \text{s})$ are listed in Table II in the case of the dynamic wave function corresponding to the initial state considered here.

These results indicate that the dynamic wave function is spread over many one-dimensional states Ψ_n^π and that the relative contribution of the two low-energy states is only 35.2%. As it appears, the one-dimensional definition (28) of the fragment yield is not pertinent, and dynamic effects should be fully taken into account to obtain realistic predictions for fragment mass distributions.

VI. CONCLUSION

In this work, we have presented a theoretical framework and numerical techniques allowing us to describe fission mass distribution in a completely microscopic way. The method is based on an HFB description of the internal structure of the fissioning system. The collective dynamics is derived from a time-dependent quantum-mechanical formalism where the wave function of the system is of GCM form. A reduction

of the GCM equation to a Schrödinger equation is made by means of the usual techniques based on the Gaussian overlap approximation. Such an approach has the advantage of describing the evolution of heavy nuclei toward fission in a completely quantum-mechanical fashion and without phenomenological parameters.

Properties of the fissioning system that have a large influence on collective dynamics have been discussed. Among them, the most important is the variation with deformation of the nuclear superfluidity induced by pairing correlations. In addition to strongly influencing the magnitude of the collective inertia, these correlations are essential in our approach because they validate the adiabatic hypothesis as a first approximation for the description of low-energy fission.

In the present application of this method to ^{238}U fission, two kinds of observables have been examined and compared to experimental data: the kinetic energy distribution and the mass distribution of fission fragments. The kinetic energy distribution, which has been derived from the mutual Coulomb energy of the fragments at scission, is found to be in good agreement with data. A small discrepancy (6%) is found around the most probable fragmentation region, which could originate from the fact that the nuclear contribution entering the mutual energy between the two fragments is not strictly zero for the corresponding scission configurations and that the attractive exchange Coulomb energy between the fragments has been neglected. Concerning fragment mass distributions, the main result of this study is that the dynamic effects taking place all along the evolution of the nucleus are essential to consider in order to obtain widths that agree with experimental data. In contrast, the maxima of the distributions are determined by the static properties of the potential energy surface in the scission region, that is, by shell effects in the nascent fragments. Finally, the influence of the choice of the initial state has been studied. In particular, symmetric fragment yields are found to be strongly influenced by the parity composition of the initial state. The quality of the results reported here encourages us to pursue further studies of fission along these lines, with some additional improvements. For instance, as suggested by the work cited in Ref. [30], we cannot exclude the fact that several valleys caused by other collective modes, such as hexadecapole or higher multipole deformation, can appear in some fissioning systems. Extensions to microscopic calculations involving three or more collective coordinates are envisaged.

ACKNOWLEDGMENTS

We thank D. Bouche, N. Carjan, and A. Rizea for useful advice concerning numerical methods and Professors F. Gönnenwein and K.-H. Schmidt for enlightening discussions on experimental results. Finally, the authors express their gratitude to Professor F. Dietrich and W. Younes for valuable discussions and for a critical review of the manuscript.

APPENDIX: HAMILTONIAN MATRIX

Starting from the functional Eq. (15), the matrix elements of the Hamiltonian matrix K can be expressed from

$$(\hat{H}_{\rm coll}g)(i,k,t) = \sum_{jl} K_{ik,jl}\; g(j,l,t), \tag{A1}$$

by writing

$$\hat{H}_{\rm coll} = \sum_{i,j=2}^{3} \hat{T}_{ij} + \tilde{V}(q_{20}, q_{30}), \tag{A2}$$

with

$$\begin{aligned} \hat{T}_{ij} &= -\frac{\hbar^2}{2}\frac{\partial}{\partial q_{i0}} B_{ij}(q_{20}, q_{30}) \frac{\partial}{\partial q_{j0}}, \\ \tilde{V}(q_{20}, q_{30}) &= V(q_{20}, q_{30}) - \sum_{i,j=2}^{3} \Delta V_{i,j}(q_{20}, q_{30}). \end{aligned} \tag{A3}$$

The different terms contributing to Eq. (A1) are

$$\begin{aligned} (\hat{T}_{22}+\hat{T}_{33})g(i,k,t) = {} & \frac{1}{4\Delta q_{20}^2}\{[-B_{22}(i-1,k) - B_{22}(i,k)]g(i-1,k,t) + [B_{22}(i-1,k) + 2B_{22}(i,k) \\ & + B_{22}(i+1,k)]g(i,k,t) + [-B_{22}(i,k) - B_{22}(i+1,k)]g(i+1,k,t)\} \\ & + \frac{1}{4\Delta q_{30}^2}\{[-B_{33}(i,k-1) - B_{33}(i,k)]g(i,k-1,t) + [B_{33}(i,k-1) + 2B_{33}(i,k) \\ & + B_{33}(i,k+1)]g(i,k,t) + [-B_{33}(i,k) - B_{33}(i,k+1)]g(i,k+1,t)\}, \end{aligned} \tag{A4}$$

$$\begin{aligned} (\hat{T}_{23}+\hat{T}_{32})g(i,k,t) = {} & \frac{1}{16\Delta q_{20}\Delta q_{30}}\{[B_{23}(i-1,k+1) + B_{23}(i,k+1) + B_{23}(i-1,k) + B_{23}(i,k)]g(i-1,k+1,t) \\ & + [B_{23}(i-1,k-1) + B_{23}(i+1,k+1) - B_{23}(i-1,k+1) - B_{23}(i+1,k-1)]g(i,k,t) \\ & + [-B_{23}(i-1,k) - B_{23}(i,k) - B_{23}(i-1,k-1) - B_{23}(i,k-1)]g(i-1,k-1,t) \\ & + [-B_{23}(i,k+1) - B_{23}(i+1,k+1) - B_{23}(i,k) - B_{23}(i+1,k)]g(i+1,k+1,t) \\ & + [B_{23}(i,k) + B_{23}(i+1,k) + B_{23}(i,k-1) + B_{23}(i+1,k-1)]g(i+1,k-1,t)\}, \end{aligned} \tag{A5}$$

and

$$\tilde{V}(i,k)\, g(i,k,t) = \{V(i,k) - \Delta V_{22}(i,k) - \Delta V_{22}(i,k) - 2\Delta V_{23}(i,k)\} g(i,k,t). \quad \text{(A6)}$$

The labels i and k are related to q_{20} and q_{30}, respectively, and Δq_{20} and Δq_{30} are the associated discretization steps. The following approximation has been used for the inertia term:

$$B_{jj}\left(i \pm \tfrac{1}{2}, k\right) \approx \tfrac{1}{2}[B_{jj}(i,k) + B_{jj}(i \pm 1, k)]. \quad \text{(A7)}$$

For products F of two functions F_1 and F_2, the following prescription has been assumed:

$$\begin{aligned} F\left(i + \tfrac{1}{2}, k\right) &= F_1\left(i + \tfrac{1}{2}, k\right) F_2\left(i + \tfrac{1}{2}, k\right) \\ &\approx \tfrac{1}{4}[F_1(i+1,k) + F_1(i,k)][F_2(i+1,k) \\ &\quad + F_2(i,k)]. \end{aligned} \quad \text{(A8)}$$

[1] M Bernas *et al*., Nucl. Phys. **A725**, 213 (2003).
[2] K. H. Schmidt *et al*., Nucl. Phys. **A665**, 221 (2000).
[3] J. Benlliure, A. R. Junghans, and K. H. Schmidt, Eur. Phys. J. A **13**, 93 (2002).
[4] P. Möller, D. G. Madland, A. J. Sierk, and A. Iwamoto, Nature **409**, 785 (2001).
[5] V. V. Pashkevich, Nucl. Phys. **A477**, 1 (1988).
[6] B. D. Wilkins, E. P. Steinberg, and R. R. Chasman, Phys. Rev. C **14**, 1832 (1976).
[7] U. Brosa, Phys. Rev. C **38**, 1944 (1988).
[8] A. V. Karpov, P. N. Nadtochy, D. V. Vanin, and G. D. Adeev, Phys. Rev. C **63**, 054610 (2001).
[9] J. W. Negele, S. E. Koonin, P. Möller, J. R. Nix, and A. J. Sierk, Phys. Rev. C **17**, 1098 (1978).
[10] J.-F. Berger, M. Girod, and D. Gogny, Nucl. Phys. **A428**, 23c (1984).
[11] J. Moreau and K. Heyde, in *The Nuclear Fission Process*, edited by C. Wagemans (CRC Press, Boca Raton, FL, 1991), p. 238.
[12] J. Decharge and D. Gogny, Phys. Rev. C **21**, 1568 (1980).
[13] J.-F. Berger M. Girod, and D. Gogny, Comp. Phys. Comm. **63**, 365 (1991).
[14] P. Ring and P. Schuck, *The Nuclear Many Body Problem* (Springer-Verlag, New York, 1980).
[15] L. M. Robledo, J. L. Egido, B. Nerlo-Pomorska, and K. Pomorski, Phys. Lett. **B201**, 409 (1988).
[16] J. Libert, M. Girod, and J.-P. Delaroche, Phys. Rev. C **60**, 054301 (1999).
[17] W. H. Press, B. P. Flannery, S. A. Teukolsky, and W. T. Vetterling, *Numerical Recipes: The Art of Scientific Computing* (Cambridge University Press, Cambridge, 1986), p. 642.
[18] N. Carjan, M. Rizea, and D. Strottman, Rom. J. Phys. **47**, 221 (2002).
[19] O. Serot, N. Carjan, and D. Strottman, Nucl. Phys. **A569**, 562 (1994).
[20] S. Pomme, E. Jacobs, K. Persyn, D. De Frenne, K. Govaert, and M.-L. Yoneama, Nucl. Phys. **A560**, 689 (1993).
[21] S. Pomme, E. Jacobs, M. Piessens, D. De Frenne, K. Persyn, K. Govaert, and M.-L. Yoneama, Nucl. Phys. **A572**, 237 (1994).
[22] F. Vives, F.-J. Hambsch, H. Bax, and S. Oberstedt, Nucl. Phys. **A662**, 63 (2000).
[23] P. Lichtner, D. Drechsel, J. Maruhn, and W. Greiner, Phys. Lett. **B45**, 175 (1973).
[24] A. C. Wahl, Los Alamos National Laboratory Report No. LA-13928, 2002 (unpublished).
[25] J. Maruhn and W. Greiner, Phys. Rev. Lett. **32**, 548 (1974).
[26] J. A. Maruhn and W. Greiner, Phys. Rev. C **13**, 2404 (1976).
[27] J. Meyer, P. Bonche, M. S. Weiss, J. Dobaczewski, H. Flocard, and P.-H. Heenen, Nucl. Phys. **A588**, 597 (1995).
[28] W. Younes and H. C. Britt, Phys. Rev. C **67**, 024610 (2003).
[29] W. Younes, private communication
[30] P. Möller, A. J. Sierk, and A. Iwamoto, Phys. Rev. Lett. **92**, 072501 (2004).